First-order periodic error correction: validation for constant and non-constant velocities with variable error magnitudes

INSTITUTE OF PHYSICS PUBLISHING MEASUREMENT SCIENCE AND TECHNOLOGY

Meas. Sci. Technol. **17** (2006) 3195–3203 doi:10.1088/0957-0233/17/12/001

First-order periodic error correction: validation for constant and non-constant velocities with variable error magnitudes

T L Schmitz[1], **D Chu**[2] **and L Houck III**[1]

[1] University of Florida, PO Box 116300, Gainesville, FL 32611, USA
[2] Agilent Technologies, Inc, PO Box 58059, Santa Clara, CA 95052, USA

E-mail: tschmitz@ufl.edu

Received 30 June 2006, in final form 9 August 2006
Published 3 November 2006
Online at stacks.iop.org/MST/17/3195

Abstract
This paper provides experimental validation of the real-time, digital first-order periodic error reduction scheme described by Chu and Ray. Measurements are completed using a single-pass, heterodyne Michelson interferometer designed to minimize common error contributors such as dead path, Abbe and environment. Motion generation over a range of velocities is achieved using an air bearing stage. Periodic error magnitude and type is varied through independent rotations of a half wave plate and polarizer located in the measurement path; experimental magnitudes for constant velocity conditions are compared to the analytical model described by Cosijns *et al*. It is shown that the correction algorithm can successfully attenuate first-order error, and identify other error orders, to sub-nm levels for a wide range of frequency mixing conditions and constant/non-constant velocity profiles.

Keywords: interferometry, heterodyne, displacement, nonlinearity, cyclic

(Some figures in this article are in colour only in the electronic version)

1. Introduction

Differential-path interferometry is often applied in situations requiring accurate displacement measurement, such as lithographic stages for semiconductor fabrication, transducer calibration, and axis position feedback for precision cutting and measuring machines. In many instances, a two-frequency (or heterodyne) Michelson-type interferometer with single, double or multiple passes of the optical paths is selected. These systems infer changes in displacement of a selected optical path by monitoring the optically-induced variation in a photodetector current. The phase measuring electronics convert this photodetector current to displacement by digitizing the phase progression of the photodetector signal. Due to non-ideal performance, mixing between the two heterodyne frequencies may occur, which results in periodic errors superimposed on the desired displacement data. First- or second-order periodic errors, with amplitudes that vary cyclically with the target position, are commonly observed. First-order periodic error, which appears as single sideband modulation on the data at a spatial frequency of one cycle per displacement fringe, often dominates. However, second-order periodic error, with a spatial frequency of two cycles per displacement fringe, is also often present.

Although modifications to traditional optical setups may be implemented to reduce periodic error, a digital correction scheme offers the advantage that no changes to the existing optical configuration are required. This paper describes experiments used to evaluate the real-time, first-order periodic error reduction scheme developed by Chu and Ray [1] for a variety of conditions. An overview of this digital logic hardware-based approach is provided in appendix A. The results described here were obtained using a single-pass, heterodyne Michelson-type interferometer that enabled: (1) isolation of periodic error as the primary uncertainty source in displacement measuring interferometry; and (2) variation of the frequency mixing that leads to periodic error so that the error magnitude could be changed. During target motion

(achieved using an air bearing stage) at various velocities, the real-time first-order error correction was digitally applied in hardware and both the uncorrected and corrected measurement signals were recorded. Various frequency mixing levels were realized by adjustment of the setup optics; the periodic error levels before and after correction are presented for multiple cases and compared to pre-correction error levels predicted by the analytical model described by Cosijns *et al* [2] for constant velocity motion profiles. Additionally, data were collected during non-constant velocity motion and the time-dependent uncorrected and corrected results are provided.

2. Background

In this work we focus on heterodyne Michelson-type interferometers. In these systems, imperfect separation of the two light frequencies into the measurement (moving) and reference (fixed) paths has been shown to produce first- and second-order periodic errors. The two heterodyne frequencies are typically carried on collinear, mutually orthogonal, linearly polarized laser beams in a method referred to as polarization coding. Unwanted leakage of the reference frequency into the measurement path, and vice versa, may occur due to a number of influences, including non-orthogonality between the ideally linear beam polarizations, elliptical polarization of the individual beams, imperfect optical components, parasitic reflections from individual optical surfaces and/or mechanical misalignment between the interferometer elements (laser, polarizing optics and targets). In a perfect system, a single frequency would travel to a fixed target, while a second, single frequency travelled to a moving target. Interference of the combined signals would yield a perfectly sinusoidal trace with phase that varied, relative to a reference phase signal, in response to motion of the moving target. However, the inherent frequency leakage in actual implementations produces an interference signal which is not purely sinusoidal (i.e., contains spurious spectral content) and leads to periodic error in the measured displacement.

Fedotova [3], Quenelle [4] and Sutton [5] performed early investigations of periodic error in heterodyne Michelson interferometers. Subsequent publications identified and described these periodic errors and built on the previous work [6–32]. Specific areas of research have included efforts to measure periodic error under various conditions (e.g., [6–9]), frequency domain analyses [10–12], analytical modelling techniques [2, 13–16], Jones calculus modelling methods [9, 17] and reduction of periodic errors (e.g., [10, 18, 30]).

3. Experimental setup

A photograph and schematic of the setup are provided in figure 1. The orthogonal, linearly polarized beams with a split frequency of approximately 3.65 MHz (helium–neon laser source) first pass through a half wave plate. Rotation of the half wave plate enables variation in the apparent angular alignment (about the beam axis) between the polarization axes and polarizing beam splitter; deviations in this alignment lead to frequency mixing in the interferometer. The light is then incident on a non-polarizing beam splitter (80% transmission) that directs a portion of the beam to a fibre optic pickup after passing through a fixed angle sheet polarizer (oriented at 45° to the nominal laser orthogonal polarizations). The pickup is mounted on a two rotational degree-of-freedom flexure which enables efficient coupling of the light into the multi-mode fibre optic. This signal is used as the phase reference in the measurement electronics.

The remainder of the light continues to the polarizing beam splitter where it is (ideally) separated into its two frequency components that travel separately to the moving and fixed retroreflectors. In this design, motion of the moving retroreflector is achieved using an air bearing stage. After the beams are recombined in the polarizing beam splitter, they are directed by a 90° prism through a polarizer with a variable rotation angle. Finally, the light is launched into a fibre optic pickup. This serves as the measurement signal in the measurement electronics (0.3 nm resolution for single-pass configuration).

The intent of the setup design was to minimize other well-known error contributors [19, 20, 33] and enable variation in the periodic error nature (i.e., first or second order) and magnitude. To isolate periodic error, the setup was designed with zero dead path difference (i.e., the distance between the polarization beam splitter and the moving retroreflector was equal to the distance between the polarization beam splitter and the fixed retroreflector at initialization) and small Abbe offset (25 mm). The measurement time (∼100 ms) and motion magnitude were kept small to minimize the contribution of air refractive index variations due to the environmental changes [19]. Additionally, careful alignment of the air bearing stage axis with the optical axis resulted in small beam shear.

Table 1. Summary of measurements.

Section	Description	Velocity (mm min^{-1})
Constant velocity		
4.1	Variable polarizer angle	540
4.2	Variable half wave plate angle	560
4.3	Variable polarizer angle	1390
4.4	Variable half wave plate angle	1370
4.5	Fixed polarizer/half wave plate angles	650–3000
Non-constant velocity		
4.6	Direction reversal	–

4. Experimental results

In this section, we describe the analysis procedures and provide experimental results for two primary scenarios: (1) constant velocity tests with variable half wave plate and polarizer orientations; and (2) non-constant velocity tests. For the former case, comparisons between uncorrected experimental data and analytical predictions [2] of first- and second-order periodic errors as a function of polarizer and half wave plate angles are provided as partial validation of the recorded uncorrected error levels. A summary of the measurements is provided in table 1.

4.1. Variable polarizer angle, low velocity

In these tests the half wave plate angle was held fixed at its nominal orientation and the polarizer angle was systematically

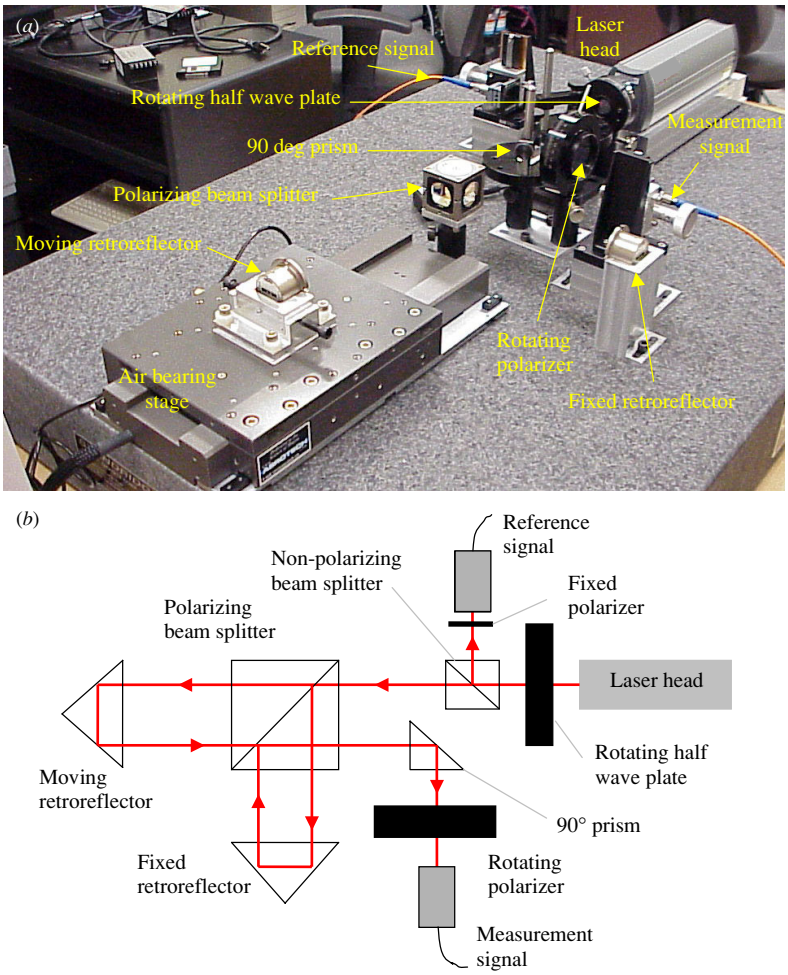

Figure 1. (*a*) Photograph of single-pass, heterodyne interferometer experimental setup. (*b*) Schematic of setup.

varied over a wide range. The velocity for the air bearing stage (and moving retroreflector) was 540 mm min^{-1}. The measurement and reference signal data from the interferometer were sampled at 312.5 kHz by the phase measuring hardware during constant velocity conditions; displacement was then determined from these signals. Output files included the uncorrected position data and the corrected data with the first-order periodic error removed using the algorithm described in appendix A.

To isolate the periodic error content (for viewing purposes) from these constant velocity tests, a least-squares linear regression was performed and the best-fit line, x_{fit}, subtracted from both the uncorrected and corrected signals. For the single-pass helium–neon interferometer setup used here, first-order error repeats every 633/2 nm = 316.5 nm, while second order completes a full cycle in 633/4 nm = 158.3 nm (although the first-order component can be described as a sum of a fundamental term and its first harmonic, which coincides with the second-order component, see equation (A.3)). To identify the first- and second-order error magnitudes, the discrete Fourier transform of the error (versus nominal displacement) was computed and the spatial frequency axis normalized to periodic error order. Typical results are shown in figure 2 where the first- and the second-order error magnitudes are 5.4 nm and 0.4 nm, respectively,

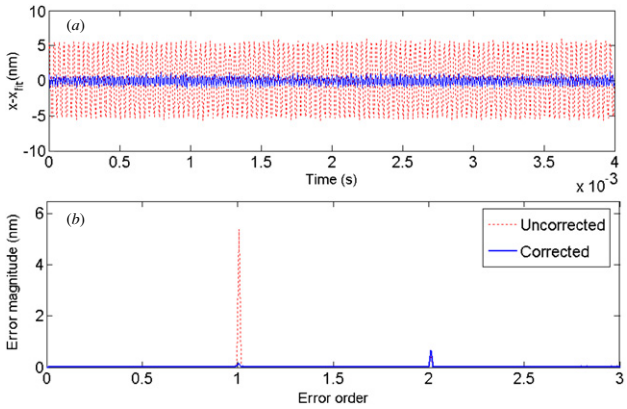

Figure 2. (*a*) Time domain uncorrected (dashed) and corrected (solid) displacement signals after removing best-fit line. (*b*) Frequency domain representation of error normalized to error order. A first-order error reduction from 5.4 nm to 0.1 nm is observed.

for the uncorrected signal. The corrected signal magnitudes are 0.1 nm and 0.7 nm, respectively.

The first- and second-order periodic error variations with polarizer angle are displayed in figure 3. Panel (*a*) shows successful attenuation of the first-order error to sub-nm levels;

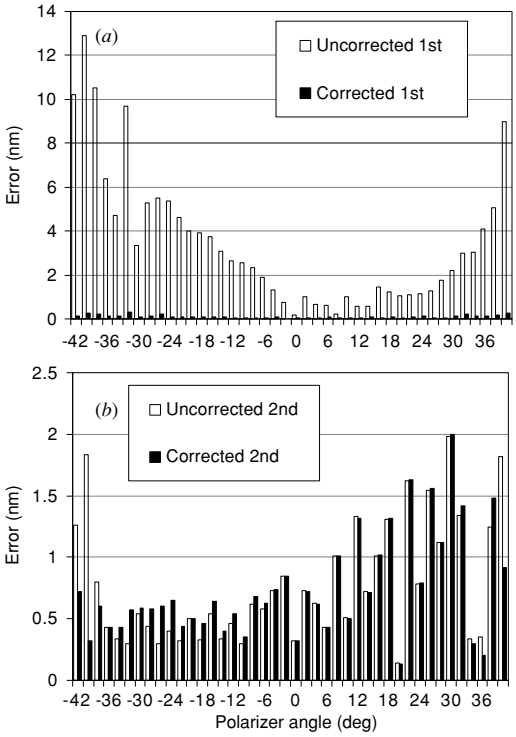

Figure 3. (*a*) First-order periodic error variation, uncorrected and corrected, with polarizer angle—540 mm min^{-1}. (*b*) Second-order periodic error variation. The 0° angle corresponds to the nominal 45° polarizer orientation.

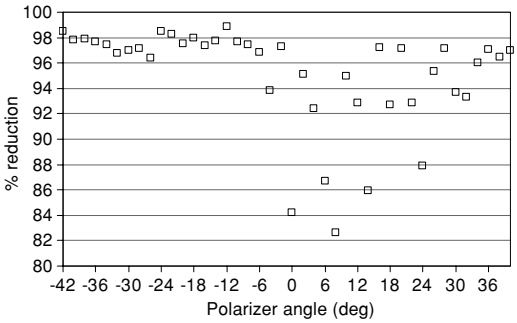

Figure 4. Per cent error reduction in first-order periodic error with variable polarizer angle—540 mm min^{-1}.

panel (*b*) shows that the algorithm does not affect the second-order error. The per cent reduction in the first-order error is provided in figure 4. Reductions of 90% or better are seen in all instances that the uncorrected first-order error was 2 nm or greater. Slightly lower percentages are observed for very small uncorrected error levels.

4.2. Variable half wave plate angle, low velocity

In this case the half wave plate angle was varied while the polarizer angle was held fixed at its nominal orientation. The stage velocity was 560 mm min^{-1}. Data collection and analysis procedures were identical to those described in section 4.1. The first- and second-order periodic error variations with half wave plate angle are displayed in figure 5. Large second-order magnitudes are observed in the bottom panel for the extreme

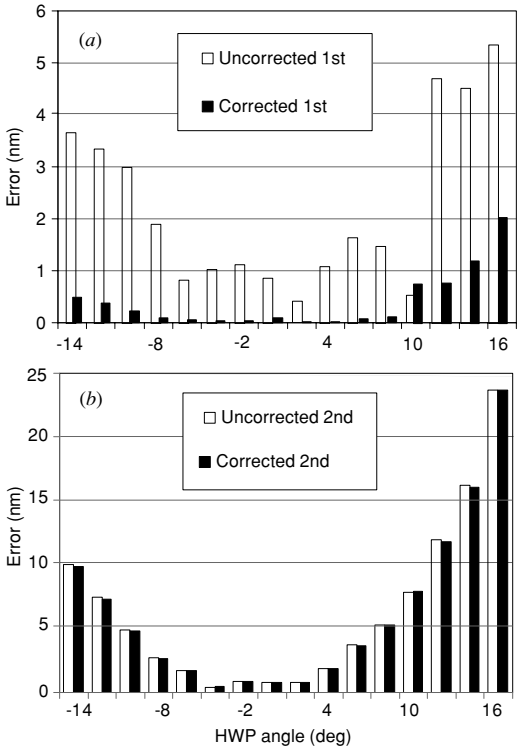

Figure 5. (*a*) First-order periodic error variation with half wave plate (HWP) angle—560 mm min^{-1}. (*b*) Second-order periodic error. The 0° angle corresponds to nominal alignment between the half wave plate fast axis and laser head vertical polarization.

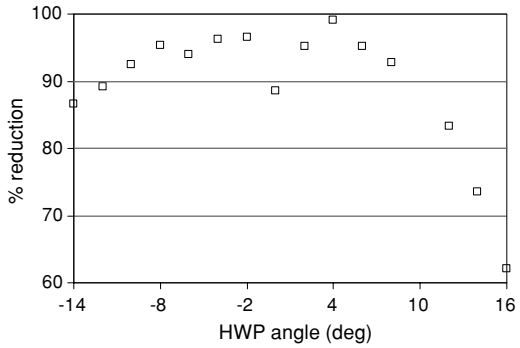

Figure 6. Per cent error reduction in first-order periodic error with variable half wave plate angle—560 mm min^{-1}. No data point is shown at 10° because the error level increased slightly (sub-nm level).

half wave plate angles. Under these conditions, the first-order error in the corrected signal increases somewhat; per cent reduction values of less than 90% are seen for deviations greater than 12° from the nominal in figure 6.

4.3. Variable polarizer angle, high velocity

Here, the half wave plate angle was held fixed at its nominal orientation and the polarizer angle was varied as in section 4.1. The stage velocity was 1390 mm min^{-1}. Significant reduction in the first-order periodic error is again observed (see figures 7, 8), where greater than 90% reduction is observed for all setups that yielded uncorrected first-order error in excess of 1 nm. The second-order result is similar to figure 3, so is not shown.

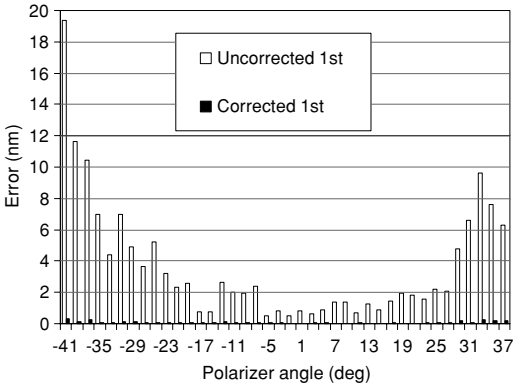

Figure 7. First-order periodic error variation (uncorrected and corrected) with polarizer angle—1390 mm min^{-1}.

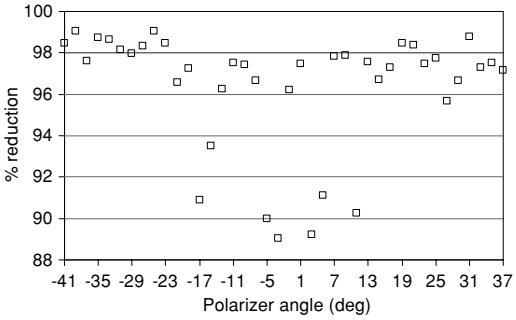

Figure 8. Per cent error reduction in first-order periodic error with variable polarizer angle—1390 mm min^{-1}.

As a check of the uncorrected measurement results, the periodic error model detailed by Cosijns *et al* [2] was used to predict the error levels for the variable polarizer angles. The Cosijns *et al* analysis propagates ellipticity of the two heterodyne (ideally linear) polarizations, non-orthogonality between the two polarizations, rotation of the polarization axes relative to the polarizing beam splitter, transmission coefficient variations for the polarizing beam splitter, and rotation of the measurement polarizer relative to the nominal 45° orientation through the interference equations to arrive at an expression for the periodic phase error, $\Delta\phi_{pe}$. See equation (1), where θ is the deviation of the polarizer angle from 45° and the variables *A*–*F* are defined in appendix B.

$$\Delta\phi_{pe} = -\tan^{-1}\left(\frac{A + B\sin(2\theta) + C\cos(2\theta)}{D + E\sin(2\theta) + F\cos(2\theta)}\right). \qquad (1)$$

The corresponding displacement error, Δl_{pe}, is given in (2), where λ is the source wavelength and n is the refractive index for the propagating medium (air in this study).

$$\Delta l_{pe} = \frac{\Delta\phi_{pe}\cdot\lambda}{4\pi n} \qquad (2)$$

Figure 9 provides comparisons between measurements and the first- and second-order error results predicted by the model for the following conditions: no ellipticity in the source polarizations, perfect polarizing beam splitter transmission, orthogonal polarizations, and a rotation of 1.5° between the laser head and polarizing beam splitter. This corresponds to a half wave plate misalignment of 0.75°. In the top panel of figure 9, the nonlinear growth in first-order error with increasing polarizer misalignment predicted by the model is

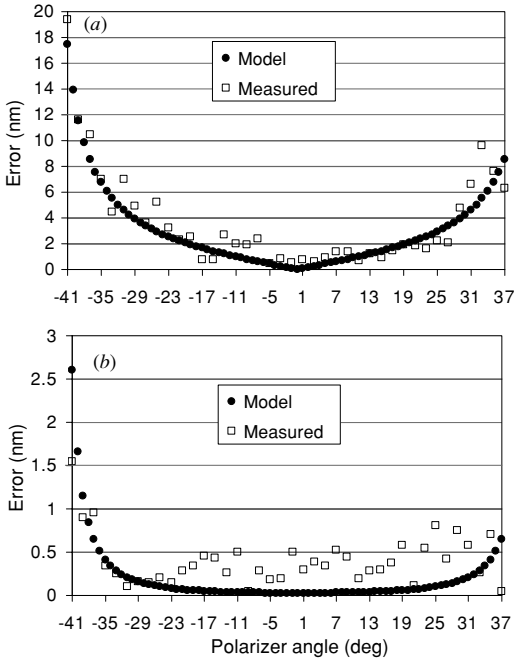

Figure 9. (*a*) Measured (uncorrected at 1390 mm min^{-1}) and modelled first-order periodic error for assumed 0.75° half wave plate misalignment and various polarizer angles. (*b*) Second-order periodic error.

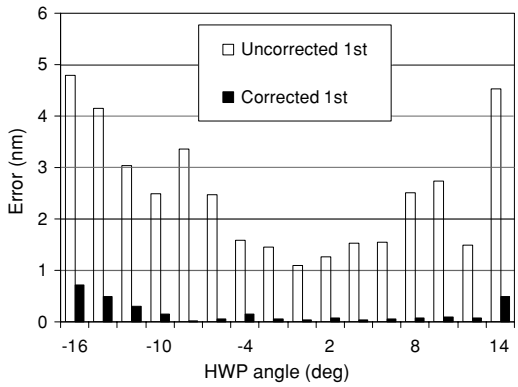

Figure 10. First-order periodic error variation, uncorrected and corrected, with half wave plate angle—1370 mm min^{-1}.

mimicked in the uncorrected data. The low sensitivity of second-order periodic error to polarizer angle is demonstrated in the bottom panel. The experimental results show larger error levels in general, but these are approaching the interferometer resolution (0.3 nm).

4.4. Variable half wave plate angle, high velocity

For these tests the half wave plate angle was again varied while the polarizer angle was held fixed at its nominal orientation. The stage velocity was 1370 mm min^{-1}. The first-order periodic error variation with half wave plate angle is displayed in figure 10. The per cent reduction in first-order error is shown in figure 11. As with the low velocity tests (figures 5 and 6), slightly reduced performance is seen at the extreme half wave plate misalignments. The second-order result is similar to figure 5, so is not included for brevity.

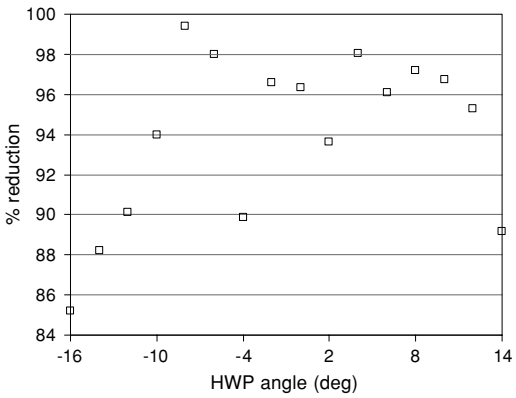

Figure 11. Per cent error reduction in first-order periodic error with variable half wave plate angle—1370 mm min^{-1}.

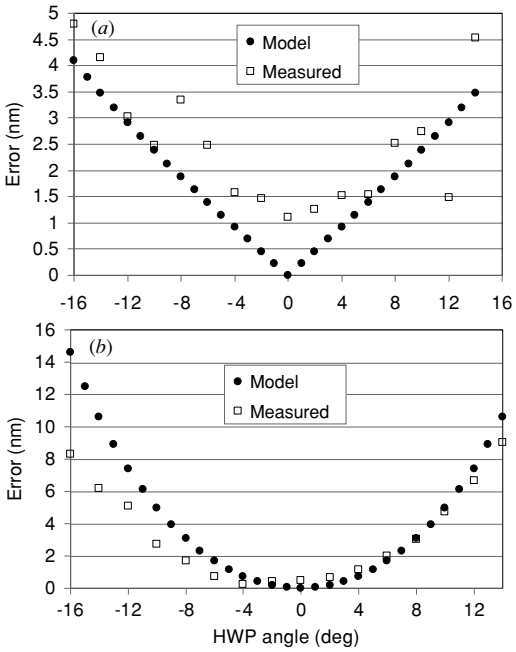

Figure 12. (*a*) Measured (uncorrected at 1370 mm min^{-1}) and modelled first-order periodic error for assumed 2° polarizer misalignment and various half wave plate angles. (*b*) Second-order periodic error.

Figure 12 shows comparisons between measurements and the first- and second-order error results predicted by the model for the following conditions: no ellipticity in the source polarizations, perfect polarizing beam splitter transmission, orthogonal polarizations, and a 2° misalignment of the polarizer from its 45° nominal orientation. The top panel shows a predicted linear growth in first-order error with half wave plate angle; the experimental data also demonstrate this trend. An approximately parabolic dependence of second-order error on half wave plate misalignment is shown by both the model and data in the bottom panel.

4.5. Additional constant velocity tests

To demonstrate the insensitivity of the digital correction algorithm to the commanded velocity, tests were also

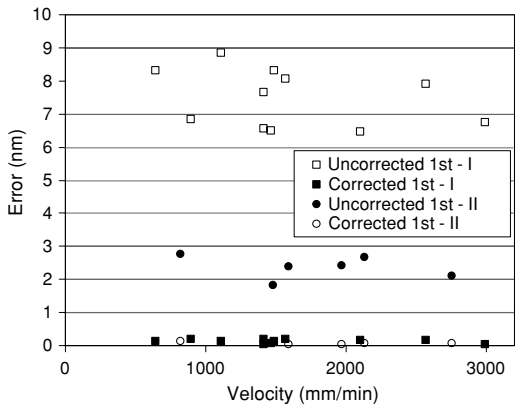

Figure 13. First-order error reduction for two optical setups (cases I and II) as a function of commanded velocity.

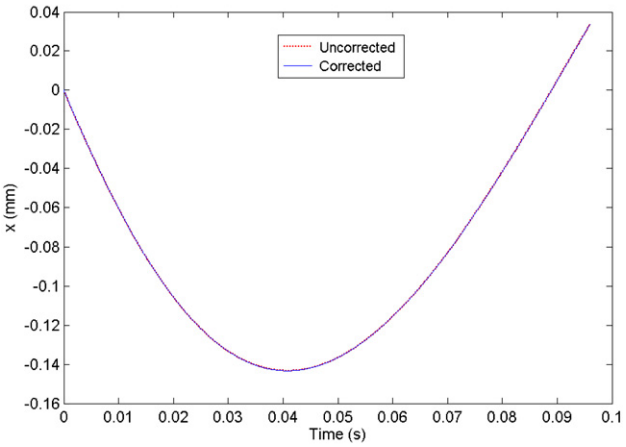

Figure 14. Macro-scale motion for direction reversal (velocity sign change).

completed using fixed optical setups with data collected at a discrete number of constant velocities. Figure 13 shows first-order error levels (uncorrected and corrected) for velocities between 650 mm min^{-1} and 3000 mm min^{-1} using two polarizer orientations (case I: 35° polarizer misalignment, case II: 15° polarizer misalignment; the nominal half wave plate angle was selected in both instances). In all tests, the per cent error reduction is greater than 95%.

4.6. Non-constant velocity

For these experiments, data were collected during non-constant velocity profiles. Misalignments of both the polarizer and half wave plate were implemented to introduce non-zero periodic error levels. Figure 14 shows an example macro-scale motion (position x versus time t) with a direction change; the velocity varied approximately linearly from −400 mm min^{-1} to +300 mm min^{-1}. For these time-varying error conditions, the Fourier analysis for periodic error level identification described in section 4.1 is not valid. However, the Chu and Ray correction algorithm accommodates motion up to constant acceleration, not just constant velocity. Furthermore, it continually estimates the periodic error magnitude and phase. The error is updated every 1.024 ms (see appendix A) and

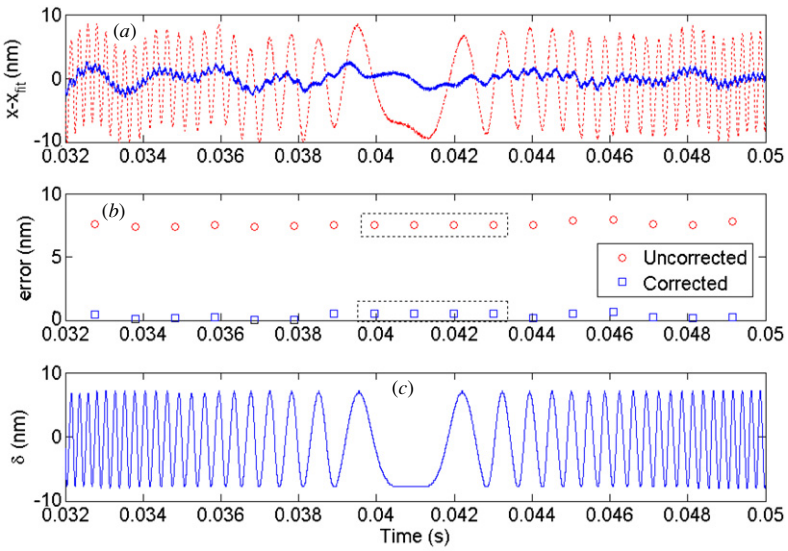

Figure 15. (*a*) Periodic error levels before and after digital correction for direction reversal and velocity sign change; dotted line is uncorrected, solid is corrected. (*b*) Correction magnitude for first-order error updated every 1.024 ms—no update is possible for the boxed points due to very low velocities. (*c*) Difference between the uncorrected and corrected signals.

used to correct the next 1.024 ms of data in a leapfrog manner. Therefore, the error magnitude is continuously available, even for non-uniform motions.

Figure 15 displays results for the time period surrounding the direction reversal and velocity sign change (∼0.0405 s) seen in figure 14, where a least-squares polynomial fit, x_{fit}, was removed from the uncorrected and corrected signals to isolate periodic error for viewing purposes and the remaining lower frequency oscillations are due to perturbations in the acceleration profile. The top panel displays the uncorrected and corrected periodic error signals. The middle panel shows the first-order error magnitudes pre- and post-correction (as noted, a new value is available every 1.024 ms). It is seen that for the boxed interval the correction magnitude does not change; updates are not possible for this very low velocity region. The bottom panel shows the difference, δ, between the uncorrected and corrected signals. This represents the time-dependent correction applied by the digital algorithm.

5. Conclusions

The tests described here showed that the real-time, Chu and Ray digital correction algorithm [1] is able to successfully reduce the first-order periodic error level to sub-nm levels in nearly all constant velocity cases. Slightly reduced performance was observed under conditions of very high second-order error (see figures 6–8, for example) as introduced with large deviations of the half wave plate orientation from the nominal angle. However, misalignments at the maximum levels tested here are unlikely in actual interferometer setups. In addition to the strong performance under constant velocity conditions, first-order error reduction for non-constant velocities was also demonstrated. It was shown that the first-order error was rapidly and effectively reduced throughout the motion profile. Finally, periodic error magnitude identification using the Chu and Ray algorithm under non-constant velocity conditions was presented.

Acknowledgments

This work was supported by Agilent Technologies, Inc., the National Science Foundation (DMI-0555645) and Aerotech, Inc.

Appendix A. Overview of digital error correction approach

A.1. Periodic error measurement

In Chu and Ray's method [1], first-order periodic error, Δs, is modelled as a periodic function of ideal position s as

$$\Delta\phi = \frac{1}{2\pi}\tan^{-1}\left[\frac{r\sin(-2\pi(\phi-\theta))}{1+r\cos(-2\pi(\phi-\theta))}\right],$$

where $\Delta\phi = \frac{2\Delta s}{\lambda}$ and $\phi = \frac{2s}{\lambda}$ are expressed in unit intervals, UI, where 1 UI $= 2\pi$ rad. This represents a single sideband (SSB) modulation of a unity magnitude main signal by a perturbing signal of fractional size r, which generates a spatially coherent disturbance of one cycle per fringe at a phase shift θ. Both quasi-static parameters r and θ are measured by a best fit regression process performed on 1.024 ms of uncorrected data (320 points at a sampling frequency of 312.5 kHz). These are immediately used to correct the following 1.024 ms of data. The measure-correct process continues in a leapfrog manner so that all but the first latent 1.024 ms of data are corrected in real time.

In measurement (but not in correction), the periodic error is modelled as a pure sinusoid. The sum of a parabola and sinusoid are best fit to a sequence of 320 position data points, expressed in UI. Macroscopic motion up to constant acceleration is removed. Therefore, excessive jerk (or the time derivative of acceleration) reduces the effectiveness of this approach. The mathematical model is expressed as:

$$\phi_j \approx x_0 + x_1 \cdot j + x_2 \cdot k + x_c \cdot \cos(2\pi\phi_j) + x_s \cdot \sin(2\pi\phi_j). \tag{A.1}$$

A column of '1's forms a unity vector, **I**. Index j steps by 1 from −159.5 to +159.5 to form a linear vector, **J**. Index k begins and ends at 16 395, stepping by $2j + 1$ (note that j starts with a negative value and ends with a positive value), to form a quadratic vector, **K**. Columns of $\cos(2\pi\phi_j)$ and $\sin(2\pi\phi_j)$ form the cosine vector **C** and the sine vector **S**, respectively. The five columns vectors **I**, **J**, **K**, **C** and **S** are combined to form a 320 × 5 matrix, **M**. These 320 equations, written in a matrix form, become $\mathbf{MX} = \mathbf{P}$, where **P** is the column of uncorrected position data and the columns of five unknowns, x_i, contained in the vector, **X**, are determined from the traditional min-squared regression solution $\mathbf{X} = (\mathbf{M^T M})^{-1}\mathbf{M^T P}$. This implies that the most effective regression operator is $\mathbf{M^T}$. Computation is immensely simplified, however, if a simpler operator $\mathbf{O^T}$ with a restricted alphabet (1, 0, −1 and −2) is chosen to mimic $\mathbf{M^T}$. The best-fit solution then becomes

$$\mathbf{X} = (\mathbf{O^T M})^{-1}\mathbf{O^T P}. \tag{A.2}$$

Simple elements enable matrix multiplications $\mathbf{O^T M}$ and $\mathbf{O^T P}$ to be synthesized using ordinary high-speed digital accumulators. The five columns of **O** are named **U**, **L**, **Q**, **E** and **D**. They are selected so that $\mathbf{U^T I} = 2^8$, $\mathbf{L^T J} = 2^{14}$, $\mathbf{Q^T K} = 2^{21}$ and $\mathbf{U^T J} = \mathbf{U^T K} = \mathbf{L^T I} = \mathbf{L^T K} = \mathbf{Q^T I} = \mathbf{Q^T J} = 0$. Matrix inversion $(\mathbf{O^T M})^{-1}$ is greatly simplified (and accelerated) by vector orthogonality and diagonal powers of 2.

For 'block regression', the columns of **O** are arranged in ten blocks of 32 identical elements expressed as: $\mathbf{U^T} = (1, 1, 0, 1, 1, 1, 1, 0, 1, 1)$, $\mathbf{L^T} = (-1, -1, 0, 0, 0, 0, 0, 0, 1, 1)$, $\mathbf{Q^T} = (1, 1, 0, 0, -2, -2, 0, 0, 1, 1)$, $\mathbf{E^T} = (e, e, e, e, e, e, e, e, e, e)$ and $\mathbf{D^T} = (d, d, d, d, d, d, d, d, d, d)$. For example, the first element, 1, in $\mathbf{U^T}$ is repeated 32 times, the second element, 1, is repeated 32 times and so on to give a total vector length of 320. The elements e and d in $\mathbf{E^T}$ and $\mathbf{D^T}$, respectively, are quantized versions of the cosine and sine functions, equalling 1 whenever the function exceeds 0.707, −1 when less than −0.707 and 0 otherwise. The periodic error magnitude V, equal to $r/(2\pi)$, and phase θ are derived from two of the five unknowns in the **X** vector, i.e., $V = \sqrt{x_c^2 + x_s^2}$ and $\theta = \left(\frac{1}{2\pi}\right)\tan^{-1}\left(\frac{x_c}{-x_s}\right)$, where the quadrant dependence of the tangent function must be observed in implementation. These parameters, in UI form, are used to correct periodic error in the next batch of data.

A.2. Periodic error correction

The SSB nature of the perturbation is taken into consideration during correction. By approximation, the periodic error in UI, $\Delta\phi = \frac{2\Delta s}{\lambda}$, can be rewritten as

$$\begin{aligned}
\Delta\phi(\phi) &= \left(\frac{1}{2\pi}\right)\tan^{-1}\left[\frac{r\sin(-2\pi(\phi-\theta))}{1+r\cos(-2\pi(\phi-\theta))}\right]\\
\Delta\phi(\phi) &\approx \frac{\left(\frac{r}{2\pi}\right)\sin(-2\pi(\phi-\theta))}{1+2\pi\left(\frac{r}{2\pi}\right)\cos(-2\pi(\phi-\theta))}\\
&= \frac{V\sin(-2\pi(\phi-\theta))}{1+2V\pi\cos(-2\pi(\phi-\theta))}\\
\Delta\phi(\phi) &\approx -V\sin(-2\pi(\phi-\theta)) + V^2\pi\sin(-4\pi(\phi-\theta)).
\end{aligned} \tag{A.3}$$

For correction convenience, the periodic error $\Delta\phi$ should be expressed as a function of the readily available uncorrected position ϕ_j, rather than the ideal position ϕ. From calculus, $\Delta\phi(x - \Delta x) \approx \Delta\phi(x) - \Delta'\phi(x)\cdot\Delta x$. Substituting ϕ_j for x and $(\phi_j - \phi$ for Δx, the calculus equation becomes $(\phi_j - \phi) \equiv \Delta\phi(\phi) \approx \Delta\phi(\phi_j) - \Delta'\phi(\phi_j)\cdot(\phi_j - \phi)$. Solving for $(\phi_j - \phi) = \frac{\Delta\phi(\phi_j)}{1+\Delta'\phi(\phi_j)}$, the correction $(\phi_j - \phi)$ becomes a function of the uncorrected position ϕ_j and not the ideal position ϕ, as desired. If only one dominant term, $-V\sin(-2\pi(\phi_j - \theta))$, is differentiated, and all harmonics higher than two are ignored, the correction simplifies to $(\phi_j - \phi) = -V\sin(2\pi(\phi_j - \theta))$. This is the correction factor used in this study. Parameters V and θ, measured from the previous 1.024 ms of position data, are used to correct every current raw position ϕ_j in a few nanoseconds. The correction has only one sine term with spatial period of $\lambda/2$. Its argument, however, is perturbed by periodic error in such a way that it almost exactly compensates for the SSB perturbation of the first-order periodic error.

Appendix B. Terms from Cosijns *et al* model

The A–F variables included in (1) are defined in (B.1)–(B.6) [2]. They are expressed as a function of the ellipticities, $\mathrm{d}\varepsilon_1$ and $\mathrm{d}\varepsilon_2$, of the two heterodyne (ideally linear) polarizations, orientation of the two beams relative to the polarizing beam splitter axes, α and β (together the two angles determine both non-orthogonality between the two polarizations and rotation of the polarization axes relative to the polarizing beam splitter), transmission coefficients, ξ and χ, for the polarizing beam splitter (ideally equal to one), and the nominal phase change, $\Delta\phi$, introduced by a given displacement, Δl. See equation (B.7).

$$\begin{aligned}
A = {} & (-(\xi^2\sin(\beta)^2 + \chi^2\cos(\beta)^2)\cos(\mathrm{d}\varepsilon_1/2)\sin(\mathrm{d}\varepsilon_2/2)\\
& - (\xi^2\cos(\alpha)^2 + \chi^2\sin(\alpha)^2)\sin(\mathrm{d}\varepsilon_1/2)\\
& \times\cos(\mathrm{d}\varepsilon_2/2))\cos(\Delta\phi) + (\xi^2\cos(\alpha)\sin(\beta)\\
& + \chi^2\sin(\alpha)\cos(\beta))\cos(\mathrm{d}\varepsilon_1/2 + \mathrm{d}\varepsilon_2/2)\sin(\Delta\phi)
\end{aligned} \tag{B.1}$$

$$\begin{aligned}
B = {} & ((\xi^2\sin(\beta)^2 - \chi^2\cos(\beta)^2)\cos(\mathrm{d}\varepsilon_1/2)\sin(\mathrm{d}\varepsilon_2/2)\\
& + (\xi^2\cos(\alpha)^2 - \chi^2\sin(\alpha)^2)\sin(\mathrm{d}\varepsilon_1/2)\\
& \times\cos(\mathrm{d}\varepsilon_2/2))\cos(\Delta\phi) + (-\xi^2\cos(\alpha)\sin(\beta)\\
& + \chi^2\sin(\alpha)\cos(\beta))\cos(\mathrm{d}\varepsilon_1/2 + \mathrm{d}\varepsilon_2/2)\sin(\Delta\phi)
\end{aligned} \tag{B.2}$$

$$\begin{aligned}
C = {} & \xi\chi(\cos(\beta)\sin(\beta)\cos(\mathrm{d}\varepsilon_1/2)\sin(\mathrm{d}\varepsilon_2/2)(1 - \cos(2\Delta\phi))\\
& + \sin(\alpha)\sin(\beta)\cos(\mathrm{d}\varepsilon_1/2)\cos(\mathrm{d}\varepsilon_2/2)\sin(2\Delta\phi)\\
& - \cos(\alpha)\cos(\beta)\sin(\mathrm{d}\varepsilon_1/2)\sin(\mathrm{d}\varepsilon_2/2)\sin(2\Delta\phi)\\
& - \sin(\alpha)\cos(\alpha)\sin(\mathrm{d}\varepsilon_1/2)\cos(\mathrm{d}\varepsilon_2/2)(1 + \cos(2\Delta\phi)))
\end{aligned} \tag{B.3}$$

$$\begin{aligned}
D = {} & ((\xi^2\sin(\beta)^2 + \chi^2\cos(\beta)^2)\cos(\mathrm{d}\varepsilon_1/2)\sin(\mathrm{d}\varepsilon_2/2)\\
& + (\xi^2\cos(\alpha)^2 + \chi^2\sin(\alpha)^2)\sin(\mathrm{d}\varepsilon_1/2)\\
& \times\cos(\mathrm{d}\varepsilon_2/2))\sin(\Delta\phi) + (\xi^2\cos(\alpha)\sin(\beta)\\
& + \chi^2\sin(\alpha)\cos(\beta))\cos(\mathrm{d}\varepsilon_1/2 + \mathrm{d}\varepsilon_2/2)\cos(\Delta\phi)
\end{aligned} \tag{B.4}$$

$$\begin{aligned}
E = {} & ((-\xi^2\sin(\beta)^2 + \chi^2\cos(\beta)^2)\cos(\mathrm{d}\varepsilon_1/2)\sin(\mathrm{d}\varepsilon_2/2)\\
& + (-\xi^2\cos(\alpha)^2 + \chi^2\sin(\alpha)^2)\sin(\mathrm{d}\varepsilon_1/2)\\
& \times\cos(\mathrm{d}\varepsilon_2/2))\sin(\Delta\phi) + (-\xi^2\cos(\alpha)\sin(\beta)\\
& + \chi^2\sin(\alpha)\cos(\beta))\cos(\mathrm{d}\varepsilon_1/2 + \mathrm{d}\varepsilon_2/2)\cos(\Delta\phi)
\end{aligned} \tag{B.5}$$

$$F = \xi\chi(\cos(\beta)\sin(\beta)\cos(\mathrm{d}\varepsilon_1/2)\sin(\mathrm{d}\varepsilon_2/2)\sin(2\Delta\phi) + \cos(\alpha)\cos(\beta)(\cos(\mathrm{d}\varepsilon_1/2)\cos(\mathrm{d}\varepsilon_2/2) - \sin(\mathrm{d}\varepsilon_1/2)\sin(\mathrm{d}\varepsilon_2/2)\cos(2\Delta\phi)) + \sin(\alpha)\sin(\beta) \times (-\sin(\mathrm{d}\varepsilon_1/2)\sin(\mathrm{d}\varepsilon_2/2) + \cos(\mathrm{d}\varepsilon_1/2)\cos(\mathrm{d}\varepsilon_2/2) \times \cos(2\Delta\phi)) + \sin(\alpha)\cos(\alpha)\sin(\mathrm{d}\varepsilon_1/2) \times \cos(\mathrm{d}\varepsilon_2/2)\sin(2\Delta\phi)) \quad \text{(B.6)}$$

$$\Delta\phi = \frac{4\pi n \Delta l}{\lambda}. \quad \text{(B.7)}$$

References

[1] Chu D and Ray A 2004 Nonlinearity measurement and correction of metrology data from an interferometer system *Proc. of 4th euspen Int. Conf. (Glasgow, Scotland, May–June 2004)* pp 300–1

[2] Cosijns S, Haitjema H and Schellekens P 2004 Modeling and verifying non-linearities in heterodyne displacement interferometry *Precis. Eng.* **26** 448–55

[3] Fedotova G 1980 Analysis of the measurement error of the parameters of mechanical vibrations *Meas. Tech.* **23** 577–80

[4] Quenelle R 1983 Nonlinearity in interferometric measurements *Hewlett-Packard J.* **34** 10

[5] Sutton C 1987 Nonlinearity in length measurements using heterodyne laser Michelson interferometry *J. Phys. E: Sci. Instrum.* **20** 1290–2

[6] Barash V and Fedotova G 1984 Heterodyne interferometer to measure vibration parameters *Meas. Tech.* **27** 50–1

[7] Bobroff N 1987 Residual errors in laser interferometry from air turbulence and nonlinearity *Appl. Opt.* **26** 2676–82

[8] Rosenbluth A and Bobroff N 1990 Optical sources of nonlinearity in heterodyne interferometers *Precis. Eng.* **12** 7–11

[9] Stone J and Howard L 1998 A simple technique for observing periodic nonlinearities in Michelson interferometers *Precis. Eng.* **22** 220–32

[10] Patterson S and Beckwith J 1995 Reduction of systematic errors in heterodyne interferometric displacement measurement *Proc. 8th Int. Precision Engineering Seminar (Compiegne, France)* pp 101–4

[11] Badami V and Patterson S 2000 A frequency domain method for the measurement of nonlinearity in heterodyne interferometry *Precis. Eng.* **24** 41–9

[12] Badami V and Patterson S 1997 Investigation of nonlinearity in high-accuracy heterodyne laser interferometry *Proc. 12th Annual American Society for Precision Engineering Conf. (Norfolk, VA)* pp 153–6

[13] Wu C and Deslattes R 1998 Analytical modeling of the periodic nonlinearity in heterodyne interferometry *Appl. Opt.* **37** 6696–700

[14] Wu C and Su C 1996 Nonlinearity in measurements of length by optical interferometry *Meas. Sci. Technol.* **7** 62–8

[15] Hou W and Wilkening G 1992 Investigation and compensation of the nonlinearity of heterodyne interferometers *Precis. Eng.* **14** 91–8

[16] Hou W and Zhao X 1994 Drift of nonlinearity in the heterodyne interferometer *Precis. Eng.* **16** 25–35

[17] Howard L and Stone J 1995 Computer modeling of heterodyne interferometer errors *Precis. Eng.* **12** 143–6

[18] Tanaka M, Yamagami T and Nakayama K 1989 Linear interpolation of periodic error in a heterodyne laser interferometer at subnanometer levels *IEEE Trans. Instrum. Meas.* **38** 552–4

[19] Bobroff N 1993 Recent advances in displacement measuring interferometry *Meas. Sci. Technol.* **4** 907–26

[20] Steinmetz C 1990 Sub-micron position measurement and control on precision machine tools with laser interferometry *Precis. Eng.* **12** 12–24

[21] Cretin B, Xie W, Wang S and Hauden D 1988 Heterodyne interferometers: practical limitations and improvements *Opt. Commun.* **65** 157–62

[22] Petru F and Cip O 1999 Problems regarding linearity of data of a laser interferometer with a single-frequency laser *Precis. Eng.* **23** 39–50

[23] Augustyn W and Davis P 1990 An analysis of polarization mixing errors in distance measuring interferometers *J. Vac. Sci. Technol.* B **8** 2032–6

[24] Xie Y and Yu Y 1992 Zeeman laser interferometer errors for high precision measurements *Appl. Opt.* **31** 881–4

[25] De Freitas J and Player M 1993 Importance of rotational beam alignment in the generation of second harmonic errors in laser heterodyne interferometry *Meas. Sci. Technol.* **4** 1173–6

[26] De Freitas J and Player M 1995 Polarization effects in heterodyne interferometry *J. Mod. Opt.* **42** 1875–99

[27] De Freitas J 1997 Analysis of laser source birefringence and dichroism on nonlinearity in heterodyne interferometry *Meas. Sci. Technol.* **8** 1356–9

[28] Li B and Liang J 1997 Effects of polarization mixing on the dual-wavelength heterodyne interferometer *Appl. Opt.* **36** 3668–72

[29] Park B, Eom T and Chung M 1996 Polarization properties of cube-corner retroreflectors and their effects on signal strength and nonlinearity in heterodyne interferometers *Appl. Opt.* **35** 4372–80

[30] Wu C, Lawall J and Deslattes R 1999 Heterodyne interferometer with subatomic periodic nonlinearity *Appl. Opt.* **38** 4089–94

[31] Oldham N, Kramar J, Hetrick P and Teague E 1993 Electronic limitations in phase meters for heterodyne interferometry *Precis. Eng.* **15** 173–9

[32] Schmitz T and Beckwith J 2002 An investigation of two unexplored periodic error sources in differential-path interferometry *Precis. Eng.* **27** 311–22

[33] Schmitz T, Evans C, Davies A and Estler W T 2002 Displacement uncertainty in interferometric radius measurements *Ann. CIRP* **51** 451–4